International Journal of Mining and Geo-Engineering

IJMGE

IJMGE 54-1 (2020) 45-50

DOI: 10.22059/ijmge.2019.253801.594725

Integration of support vector machines for hydrothermal alteration mapping using ASTER data – case study: the northwestern part of the Kerman Cenozoic Magmatic Arc, Iran

Saeed Mojeddifar [a, *], Seyed Mohammad Mavadati [b]

[a] *Department of Mining Engineering, Arak University of Technology, Arak, Iran*

[b] *Department of Electrical & Computer Engineering University of Denver, Denver, Co, USA*

Article History:

Received: 12 March 2018,

Revised: 09 April 2019

Accepted: 12 July 2019.

ABSTRACT

This work applies support vector machine (SVM) algorithms in two versions of singular and general SVM classifiers to map hydrothermal alteration zones in the northwestern part of the Kerman Cenozoic Magmatic Arc (KCMA). Three visible bands and six SWIR bands of ASTER images were applied as inputs for SVM classifiers. The developed algorithms were able to classify ASTER images into hydrothermal alteration or non-hydrothermal alteration classes. In singular SVM, nine classifiers were able to vote individually for every pixel in the image. Then, they were combined through integration rules to present a final decision about every pixel. The general SVM classifier integrated nine ASTER bands at the signal level to produce the final decision. The classification error rate showed that the general Gaussian RBF kernel-based SVM classifier had higher accuracy for the classification of hydrothermal alteration zones. The SVM results were then compared with other classified images based on band ratio and SAM methods. The main problem associated with these methods was that vegetation covering was highlighted as alteration zones while the SVM algorithm could solve this issue. Also, the verification of results, based on field and laboratory investigations, showed the SVM method to produce a more accurate map of alteration than that obtained from the band ratio and SAM.

Keywords : *Hydrothermal alteration, ASTER, Support vector machine, Band ratio, Spectral angle mapper*

1. Introduction

Remote sensing science applies spectral signatures of minerals to discriminate different rock types. Various attempts have been made to distinguish altered pixels using remote sensing methods [1, 2, 3, 4, 5, 6, 7, 8, 9]. Hydroxyl-bearing minerals are important products of hydrothermal alteration. Clays, which contain Al-OH- and Mg-OH-bearing minerals, are distinguished by an absorption peak in the 2.1–2.4 μm (Fig. 1). On the other hand, the presence of water in vegetative tissues commonly may cause spectral interference with hydroxyl-bearing minerals in the 2.1–2.4 μm (Fig. 1). Therefore, the discrimination between vegetation and hydroxyl-bearing minerals is a significant challenge in remote sensing.

According to recent studies, differentiation between various alteration minerals and vegetation cover is difficult when using some image-processing techniques such as band ratio, principal component analysis, and spectral angle mapper. For example, Abrams et al. [1] attempted to identify hydrothermal alteration using digitally processed aircraft multispectral images. Kaufmann [2] applied TM images to map hydrothermal alteration zones. Knepper and Simpson [3] used TM color ratio composite images to detect hydrothermally-altered rocks. Bennett et al. [4] integrated TM data with field and laboratory data to discover alteration zones. Goosens and Kroonenberg [5] used TM ratio images to identify rocks overlain by residual soil. Carranza and Hale [6] mapped hydrothermal alteration with integrating results of TM images and ground data. Porwal et al. [7] implemented a neuro-fuzzy algorithm to provide a mineral potential map. Honarmand et al. [8] applied principal component analysis and spectral angle mapper to discover hydrothermal alteration minerals.

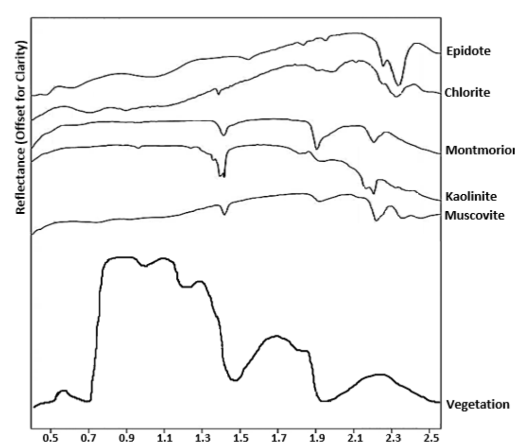

Fig. 1. Reflectance signature of common hydrothermal minerals vs. vegetation cover.

Bodraddoza and Fujimitsu [9] tried to detect alteration zones using color composite, band ratio, principal component, least-square fitting, and reference spectra analysis. Another challenge about the traditional methods, such as band ratio and spectral angle mapper, is the erroneous

---

* Corresponding author. Tel: +98-9153054931. *E-mail address:* mojeddifar@arakut.ac.ir (S. Mojeddifar).

classification of unaltered materials as hydrothermal alteration areas. The present work employs the ASTER data by applying different support vector machine (SVM) algorithms integrated with fusion rules to solve this issue. SVM is an efficient technique for data classification. The theory of SVM is based on the idea of structural risk minimization (SRM)[10]. In many applications, SVM has been shown to provide higher performance than that usually obtained from traditional learning machines. It has been proved to be a powerful tool for solving classification problems [11]. The dataset used in this study contains three ASTER scenes using SWIR and VNIR bands, covering Meiduk porphyry copper deposit, Kader, Abdar, and Iju mineral prospects located in the Kerman Province, in southeastern Iran.

2. Geology of the Area

The case study is a part of the Iranian Cenozoic Magmatic Belt (CICMB), which lies parallel to the Zagros geo-suture for about 1800km from Western Azerbaijan (northwest of Iran) to the north of Makran (southeast of Iran). The CICMB is part of the Alpine-Himalayan orogenic belt, which extends from western Europe to Turkey, across Iran into western Pakistan [12]. Igneous activity in this zone commenced in the Eocene and continued to its climax during the mid-Eocene volcanic eruptions and Oligo-Miocene plutonic intrusions in many parts of Iran [13, 14]. The study area is located in the Kerman Cenozoic Magmatic Arc (KCMA), which is a part of the southeast sector of the CICMB. The KCMA forms a northwest-southeast trending magmatic arc segment, about 400 km long and 40-50 km wide along the southern margin of the central Iran micro-continent. The geology of the Kerman arc segment mainly consists of an Upper Cretaceous–Eocene basic to felsic volcanic–sedimentary complex. The Oligo-Miocene granitic rocks intruded into thick sequences (15 km thick) of Eocene lava, pyroclastic, and volcaniclastic rocks, as well as batholiths, stocks, and dikes [15].

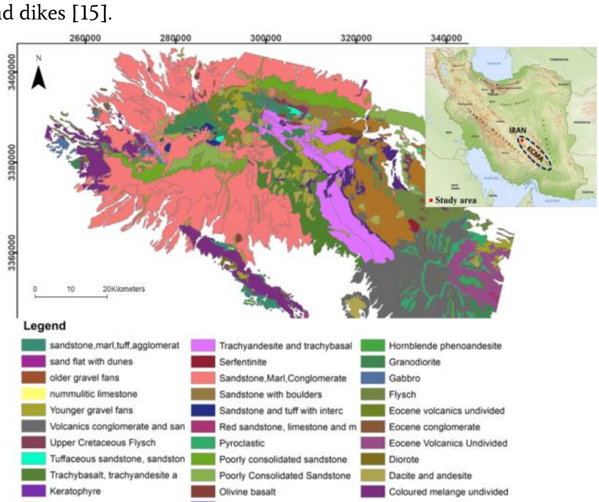

Fig. 2. Geologic map of the study area [16]. The location of the area is also shown on the Kerman Cenozoic magmatic Arc.

The Cretaceous colored mélange is the oldest, and the Quaternary alluvial deposits and gravel fans are the youngest exposures in the study area (Fig. 2). Cretaceous sediments are mainly of flysch successions. Eocene volcanic rocks are subdivided into the Bahr-e-Aseman complex and the Lower, Middle, and Upper Razak complexes. These rocks are represented by pyroclastics, pyroxene trachyandesites, trachyandesites, trachybasalts, tuffaceous sediments, basaltic rocks, and (pyroxene) andesites. The sedimentary rocks in the volcanic-sedimentary complex are mainly sandstone and, less frequently, limestone. The Eocene volcanic sedimentary rocks are intruded by the Oligocene-Miocene plutons that consist of granodiorite, quartz-diorite, diorite, monzonite, tonalite, and granite. The volcanic rocks near these intrusive suites are widely metamorphosed and altered. Most of the plutonic and volcanic rocks are hydrothermally altered and mineralized in places. Argillization, sericitization, and propylitization are the most common types of hydrothermal alteration in the area. The Neogene sediments consist mainly of loosely consolidated, unsorted, and poorly stratified conglomerate and sandstone overlying the Eocene volcanic-sedimentary rocks. Calcareous terraces and recent alluvium deposits are the main sedimentary units formed in the Quaternary. The Dehaj and Aj phases of volcanic activity in the form of pyroclastic, dacite, and basaltic rocks occurred in the Pliocene. The Meiduk, Abdar, Kader, Godekolvari, Iju, Serenu, Chahfiroozeh, Parkam, are the known copper deposits in this area [17].

3. Support Vector Machine Overview

The foundations of Support Vector Machine (SVM) were developed by Vapnik [10] and have been applied to many pattern recognition applications such as classification and regression problems. SVM classifiers use an optimal hyperplane that maximizes the distance between the margins of two classes by a small number of training samples (support vectors). An SVM is a linear binary classifier (Fig. 3) that cannot classify the patterns in which data points of different classes overlap each other. Therefore, the kernel-based SVM would be applied to represent more complex shapes than linear hyperplanes. Suppose, in a binary classification problem, N training samples ($x_i \in R^d$, ($i=1,2,\ldots,N$)) are applied to train the SVM classifier. The aim is to find a surface for categorizing all of x_i to the corresponding∈∈ class $y_i \in \{-1,+1\}$. This surface is defined by $w \in R^d$ (normal to hyperplane) and $b \in R$ (the amount of bias for classifying the data without errors). The decision rule is based on $\mathrm{sgn}[f(x)]$, where $f(x)$ is the discriminant function associated with the linear surface and defined as:

$$f(x) = w.x + b \tag{1}$$

The SVM classifier searches to estimate w and b so that:

$$y_i (w \bullet x_i + b) > 0 \text{ with } i = 1,2,\ldots,N \tag{2}$$

The maximum distance between the closest training samples and the separating surface is used to find the best discriminant hyperplane. When rescaling hyperplane parameters (w,b), it is possible to demonstrate the distance by $\frac{1}{\|w\|}$:

$$\min yi (w \bullet xi + b) \geq 1, i = 1,2,\ldots,N \tag{3}$$

The margin between the two classes is $\frac{2}{\|w\|}$, and the optimal hyperplane is determined by solving the quadratic programming problem:

$$\begin{cases} Minimizing : \frac{1}{2}\|w\|^2 \\ subject\ to : y_i \ (w \bullet x_i + b) \geq 1, \ i = 1,2,..,N \end{cases} \tag{4}$$

For solving the above classical optimization problem, the following dual problem could be solved using the Lagrange formulation:

$$\begin{cases} Minimize : \sum_{i=1}^{N} \alpha_i - \frac{1}{2} \sum_{i=1}^{N} \sum_{j=1}^{N} \alpha_i \alpha_j y_i y_j (x_i \bullet x_j) \\ subject\ to : \sum_{i=1}^{N} \alpha_i y_i = 0 \ and \ \alpha_i \geq 0, i = 1,2,\ldots,N \end{cases} \tag{5}$$

Quadratic programming (QP) is applied to estimate the Lagrange multipliers, [18]. The calculated discriminant function is associated with the optimal hyperplane, depends on both the Lagrange multipliers and the training samples, i.e.

$$f(x) = \sum_{i \in S} \alpha_i y_i (x_i . x) + b \tag{6}$$

Where S is the subset of training samples corresponding to the non-zero Lagrange multipliers. The Lagrange multiplier effectively weights each training sample based on its importance for the discriminant function. The training sample with non-zero weights are called the support vectors and they lie precisely at the distance of $\frac{1}{\|w\|}$ to the optimal separating hyperplane.

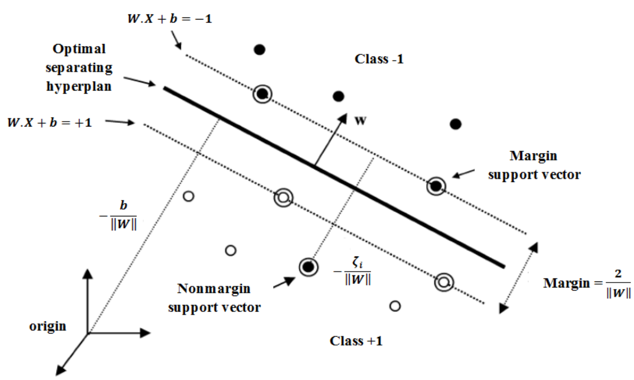

Fig. 3. The structure of SVM hyperplane. White and black circles refer to the classes "+1" and "-1," respectively [19].

4. Fusion of Multispectral Information

In many practical applications, a given source or sensor information comprises redundancy. Also, the information obtained by different tools provides complementary details about the objects. Removing the redundant information and finding the complementary parts is the final goal of the fusion approaches [20]. In remote sensing, the integration of multispectral data has been practiced to visualize target pixels. The current study attempts to detect the purest pixels representing alteration minerals using different integration levels. Employing the information of all ASTER bands requires the combination of useful and complementary information and then making a final decision. The pixels of ASTER bands could be integrated at four different levels:

(a) signal-level integration
(b) feature-level integration
(c) matching-score-level integration
(d) decision-level integration

It is generally believed that a combination of integration levels as early as possible is more effective in a recognition system [21]. Thus, the present work applies signal and decision levels and compares the efficiency of each method based on the error rate of SVM classifiers. While integrating multispectral information at the signal level, the information is first concatenated, and then, a multi-dimensional image is produced accordingly. Afterward, a classifier is designed to categorize each pixel into a specific class. In the decision level, a special classifier is designed for each band, and the fusion rules (i.e., AND, OR, and VOTING) are applied to make a final decision about the class of pixels.

5. Experiments and Results

The performance of the developed SVM classifier is calculated based on the classification error rate. The classification error rate is computed based on averaging two errors: 1) false acceptance error (FA); 2) false rejection error (FR):

$$\text{Classification Error} = \frac{FA + FR}{2} \tag{13}$$

This study uses signal- and decision- level algorithms to improve the performance of classifiers, and finally, the best classifier is employed to the whole image to classify the image into two classes; hydrothermal alteration and non-hydrothermal alteration classes.

5.1. ASTER Image

ASTER is an advanced multispectral satellite imaging system that was launched onboard NASA's Terra spacecraft in December 1999. ASTER covers the VNIR (0.52 to 0.86 µm), SWIR (1.6 to 2.43 µm) and TIR (8.125 to 11.65 µm) spectral regions with 14 channels with high spatial, spectral and radiometric resolution [22, 23]. The swath width is 60 km, but the pointing capability extends to 232 km, and the spatial resolution varies with wavelength region. This work applied three ASTER level 1B scenes. Two scenes were acquired on 18th April 2000 and another scene on 15th June 2007. These scenes were georeferenced by using an orthorectified ETM^{+} image, in the UTM projection and WGS-84 ellipsoid as a datum. The first two were corrected for Crosstalk. Atmospheric corrections were also performed by using Fast Line of Sight Atmospheric Analysis of Spectral Hypercubes (FLAASH). The datasets were then mosaicked. The Internal Average Relative Reflectance (IARR) correction was also applied. Fig. 4 shows a false-color composite of ASTER bands 231(RGB) of the study area.

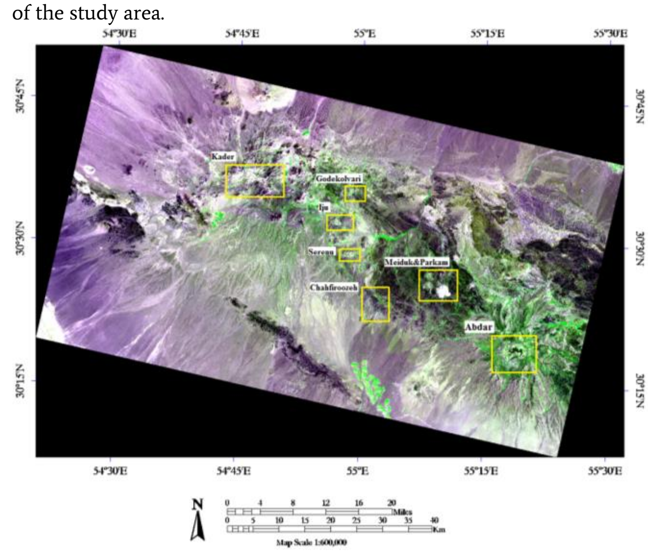

Fig. 4. Color composite of ASTER images (band 2 in red, band 3 in green, and band 1 in blue). The vegetation cover is shown in green color. The yellow rectangles indicate the important copper deposits in the area.

5.2. Configuration

The train and test pixels are required for developing the SVM classifier. The authors analyzed the study area and clearly determined two classes of alteration and non-alteration in the region illustrated in Fig. 5. The whole image (Fig. 5) contains 551289 pixels, and the training polygons contain 3776 pixels. Polygons 1 and 2 represent the hydrothermal alteration regions that include 644 pixels, and polygons 3, 4, and 5 are non-hydrothermal alteration regions that have 3132 pixels. This research randomly selected 80% of pixels of polygons to train the SVM classifier, and the remaining data were used to investigate the performance of the developed classifier.

5.3. Classification Results:

The VNIR + SWIR spectral regions of ASTER data (3 + 6 bands) were applied to implement the SVM classifier. The applied SVM can categorize image pixels into hydrothermal alteration or non-hydrothermal alteration classes. This procedure is divided into two phases until reaching the goal. In the first phase, the SVM algorithm is implemented based on each band (singular SVM). It means that nine SVM classifiers are able to vote individually for every pixel in the image. Then, all votes are combined through the integration rules to present a final decision about every pixel. In the second phase, the spectral values of nine bands in each pixel are integrated at the signal level, and a nine-dimensional image is produced by concatenating the ASTER bands (general SVM). Then, the structure of the SVM algorithm can be constructed using different structures (Linear and Nonlinear).

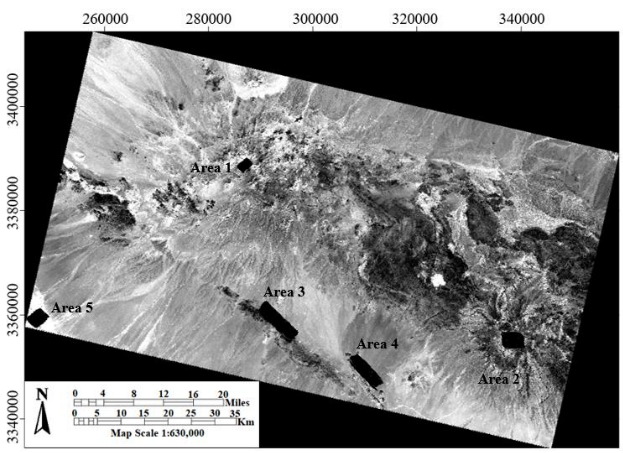

Fig. 5. Training and testing areas used for image classification (see the text).

5.3.1. Singular SVM Classifiers

In the first phase, this work intends to develop the SVM algorithm based on each ASTER band. It means that nine different SVM classifiers are provided to make nine binary decisions for every pixel (0 for hydrothermal alteration and 1 for non-hydrothermal alteration). The SVM algorithms were programed using the MATLAB software in linear and nonlinear modes. The Gaussian RBF kernel was used to construct the nonlinear algorithms. Sub-band SVM classifiers were evaluated using a test dataset. Table 1 and 2 shows the classification error rate of linear and Gaussian SVM algorithms, respectively. The obtained results indicate that the SVM classifiers of band 4 and band 7 could classify the test dataset with higher accuracy when both classes are considered. Since most of the alteration minerals show a maximum peak at range of 1.6-1.7 μm (band 4) and a minimum peak at a range of 2.23-2.28 μm (band 7), the related SVM classifiers could present better results compared to other classifiers. If the results of SVM classifiers of classes 1 and 2 are individually considered, the error rate of the SVM classifiers of band 4 and band 7 will increase. Therefore, we decided to integrate all of the nine classifiers using three decision rules (AND, OR, VOTING) to develop the final SVM classifier. Fig. 6 illustrates the block diagram of the described phase. The performance of the final SVM classifiers based on fusion rules shows that the best integration is obtained when the rule AND is applied.

Table 1. Classification results of singular SVM classifiers (Linear).

Classification Error Rate (%)	SVM classifier for each ASTER Band								
	1	2	3	4	5	6	7	8	9
Total	76.58	39.41	83.21	22.48	40.87	55.02	27.51	42.19	44.31
class 1	7.69	66.66	11.02	47.86	46.15	47.00	51.28	48.71	43.58
class 2	89.20	34.42	91.07	17.84	39.90	56.49	23.16	41.00	44.44

Table 2. Classification results of singular SVM classifiers (Gaussian RBF).

Classification Error Rate(%)	SVM classifier for each ASTER Band								
	1	2	3	4	5	6	7	8	9
Total	25.79	27.77	59.92	21.03	44.70	76.05	28.43	53.43	46.69
class 1	86.29	75.80	20.96	45.16	25.80	14.51	36.29	24.19	25.00
class 2	13.92	18.35	67.56	16.29	48.41	88.13	26.89	59.17	50.94

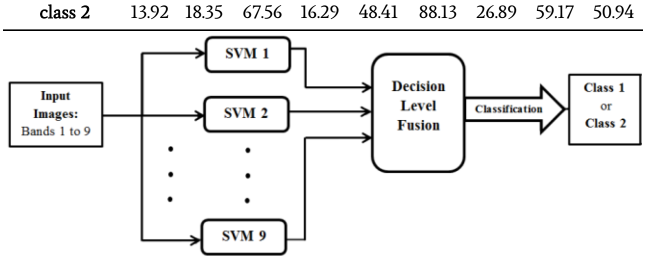

Fig. 6. Block diagram of singular SVM classifiers.

Table 3. Decision-level fusion of singular SVM classifiers (Linear and Gaussian RBF).

Classification Error Rate (%)	Linear SVM	RBF SVM
AND	15.47	16.40
OR	57.40	71.16
VOTING	39.81	40.21

5.3.2. General SVM Classifier

In the second phase, only one SVM classifier is developed to map alteration regions; therefore all of the nine ASTER bands are integrated at the signal level to obtain the final decision for every pixel (Fig. 7). The test dataset evaluated the general SVM classifier. Table 4 presents the results of linear and nonlinear (RBF) classifiers. Comparing Tables 3 and 4 shows that the general SVM classifier can classify better than the singular one, and the performance of the general SVM classifier based on the RBF kernel is much reliable than the Linear SVM. Therefore, the general SVM classifier based on the Gaussian RBF kernel was used to categorize the whole image into two classes (Fig. 8).

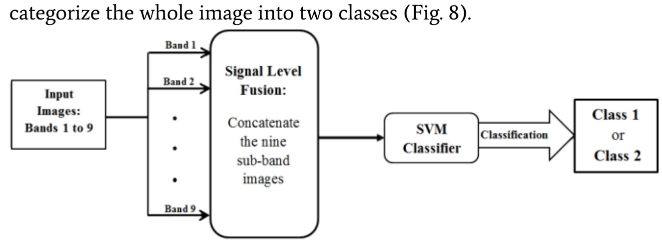

Fig. 7. Block diagram of the general SVM classifier.

Table 4. Signal-level integration of the general SVM classifier (Linear and Gaussian RBF).

Classification Error Rate (%)	Linear SVM	RBF SVM
Total	2.69	1.69
Region 1	4.58	3.33
Region 2	2.31	1.35

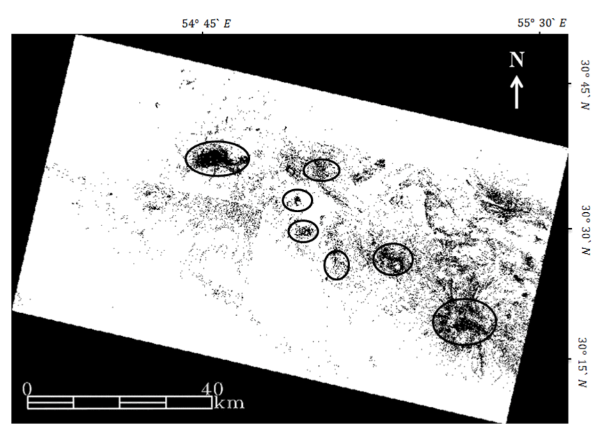

Fig. 8. Classified hydrothermal (Black) and non-hydrothermal (White) regions by the general SVM (Gaussian RBF).

6. Discussion

Based on the classification error rate (Tables 4 and 5), the general SVM classifier based on the Gaussian RBF kernel was selected to classify the study area into hydrothermal alteration (black) and non-hydrothermal alteration (white) regions (Fig. 8). The main goal was to detect hydrothermal alteration regions in the study area for the exploration of porphyry copper deposits. Iju, Serenu, Chahfiroozeh, Meiduk, Parkam, Kader, and Abdar are the known porphyry copper deposits, and according to Fig. 8, the developed algorithm could identify these deposits. The black polygons represent the location of each known deposit, and more details about the known deposits are illustrated in Fig. 4. The results of the general SVM classifier were compared with those of conventional techniques such as spectral angle mapper and band ratio methods. In addition, further verification was also considered through thin section examination and X-ray diffraction results presented by Mojedifar et al. [25] and Honarmand et al. [8]. They investigated the altered areas in both the field and the laboratory. Their studies showed that sericite alteration was dominant at the Iju, Serenu, Chahfiroozeh, Meiduk, Parkam, Kader, and Abdar porphyry copper deposits. Two types of phyllic alteration could be recognized in the field, including ferric-iron-rich and iron-oxide poor phyllic alterations. The iron-oxide-rich phyllic zone showed a large number of iron oxide minerals on the surface. The common secondary minerals at the Kader, Iju, Serenu, Parkam, Meiduk, and Abdar deposits are in the form of goethite, jarosite, and minor hematite in three hydrothermal alteration zones of phyllic, argillic, and propylitic. Since discriminating clay minerals in thin sections was difficult, they analyzed the rock samples by a spectroradiometer. Argillic alteration is present in the deposits at Kader, Serenu, Meiduk, Parkam, Godekolvary, and Abdar. Propylitic alteration happens around most of the mineralized areas. They also studied the samples by a spectroradiometer. Based on their study, in the Kader area, the three hydrothermal alteration zones were relatively uniform over an area that included the phyllic, argillic, and propylitic alteration zones. Argillic alteration is present in the deposits at Kader, Meiduk, Parkam, and Abdar. The spectra of propylitic rocks indicated strong absorption in 2.33 µm because of the presence of chlorite and epidote (Fig. 9). A comparison of the altered areas in Fig. 8 with field data revealed that the general SVM classifier could identify alteration zones, acceptably.

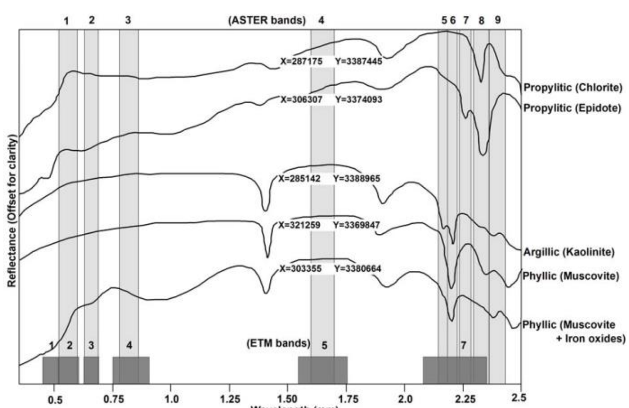

Fig. 9. The spectra of the samples from phyllic, argillic, and propylitic zones, measured by a field spectroradiometer. The UTM, Zone-40 coordinates of the samples are illustrated on the spectra [8, 25].

ASTER images were also analyzed with the band ratio and spectral angle mapper (SAM) techniques in order to compare their results with the SVM classified image. SAM determines the spectral similarity between image pixels and reference spectra of alteration minerals through calculating the angle between them. This research used the reference spectra of muscovite driven by the USGS library to map the phyllic and argillic alteration zones (Fig. 10a). Also, band ratio (5+7)/6 was calculated to map phyllic alteration areas that were exposed as bright pixels in Fig. 10b. A comparison of the SVM output (Fig. 8) with altered areas mapped through SAM (Fig. 10a) revealed that the vegetation cover was highlighted as alteration zones by SAM, black ellipses in Fig. 10a, while this issue was solved in the classified image obtained by SVM (Fig. 8). Also, the band ratio approach presented similar errors to those produced by the SAM method (Fig. 10b). Therefore, the general SVM classifier could be considered as an exploration tool in areas with similar climate and geology to those of the present study area.

7. Conclusion

The present research developed SVM algorithms in two versions of singular and general SVM classifiers to map hydrothermal alteration zones. The classification error rate showed that the general SVM algorithm could detect alteration minerals with higher accuracy. The reason could be found in the structure of developed classifiers. The general SVM classifies each pixel of the ASTER image using nine bands at the same time, while the singular SVM algorithm classifies each pixel individually based on every ASTER band. It means that the singular SVM presents nine classified images, and then they are integrated using integration rules. The classification error rate indicated that the general SVM based on the Gaussian RBF kernel could present the best results with an error value of 1.69%. The singular SVM showed that the best results were achieved when it used the ASTER bands known as the spectral signature of alteration minerals such as band 4 (with spectral resolution 1.6-1.7 µm). A comparison of the obtained results with traditional methods was performed in order to evaluate SVM classifiers. The general SVM based on the RBF method could successfully detect known deposits comprising alteration minerals in the study area. Also, the developed algorithm could differentiate alteration zones from the vegetation cover while SAM and band ratio methods highlighted vegetation as alteration regions. Therefore, this method is suggested for the exploration of hydrothermal alteration in other parts of the Iranian Cenozoic magmatic belt.

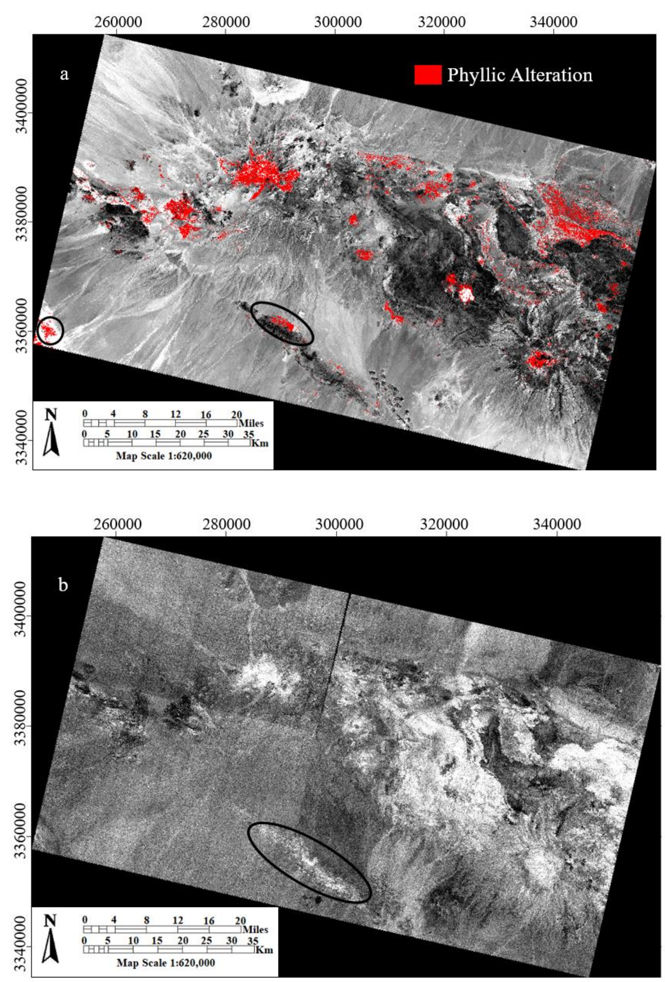

Fig. 10. (a): The result of SAM classification for phyllic alteration, overlain on ASTER band 1 image; (b): Phyllic alteration map by the band ratio method, the black ellipses, and the circle indicates alteration areas at the vegetation cover and sedimentary rocks, respectively.

Conflict of Interest: The authors declare that they have no conflict of interest.

REFERENCES

[1] Abrams MJ, Brown D, Lepley L, Sadowski R, Remote sensing for porphyry copper deposits in southern Arizona. Economic Geology, 1983, 78:591–604.

[2] Kaufmann H, Mineral exploration along the Aqaba–Levant structure by use of TM data; concepts, processing, and results. Int. J. Remote Sensing, 1988, 9:1639–1658.

[3] Knepper DH, Simpson SL, Remote sensing in Geology and mineral resources of the Altiplano and Cordillera Occidental, Bolivia, U.S. Geol. Surv. Bull. 1975, 47–55.

[4] Bennett SA, Atkinson WW, Kruse FA, Use of thematic mapper imagery to identify mineralization in the Santa Teresa District, Sonora, Mexico. Int. Geol. Rev. 1993, 35:1009–1029.

[5] Goosens MA, Kroonenberg SB, Spectral discrimination of contact metamorphic zones and its potential for mineral exploration, province of Salamanca, Spain. Remote Sensing of the Environment, 1994, 47:331–344.

[6] Carranza EJM, Hale M, Mineral imaging with LANDSAT thematic mapper data for hydrothermal alteration mapping in heavily vegetated terrane. In: International journal of remote sensing, 2002, 23: 4827-4852.

[7] Porwal A, Carranza EJM, Hale M, A Hybrid Neuro-Fuzzy Model for Mineral Potential Mapping. Mathematical Geology, 2004, 36:803-826.

[8] Honarmand M, Ranjbar H, Shahabpour J, Application of Spectral Analysis in Mapping Hydrothermal Alteration of the Northwestern Part of the Kerman Cenozoic Magmatic Arc, Iran. Journal of Sciences, 2011, 22: 221-238.

[9] Bodruddoza MD, Fujimitsu Y, Mapping hydrothermal altered mineral deposits using Landsat 7 ETM+ image in and around Kuju volcano, Kyushu, Japan. Journal of Earth System Science, 2012, 121:1049–1057.

[10] Vapnik V, The Nature of Statistical Learning Theory. Springer, New York, 1995.

[11] Burges CJC, A tutorial on support vector machines for pattern recognition.Data Mining Knowl. Discov, 1998, 2:121–167.

[12] Shafiei B, Haschke M, Shahabpour M, Recycling of orogenic arc crust triggers porphyry Cu mineralization in Kerman Cenozoic arc rocks, southeastern Iran. Mineraiuml Deposita, 2009, 44(3):265-283.

[13] Alavi M, Tectono-stratigraphic evolution of the Zagros-sides of Iran. Geology, 1980, 8(3):144–149.

[14] Shahabpour J, Aspects of Alteration and Mineralization at the Sar-Cheshmeh Copper–Molybdenum Deposit, Kerman, Iran. Unpublished PhD Thesis, Leeds, University of Leeds, 1982.

[15] Boomeri M, Nakashima K, Lentz DR, The Miduk porphyry Cu deposit, Kerman, Iran: A geochemical analysis of the potassic zone including halogen element systematics related to Cu mineralization processes. Journal of Geochemical Exploration, 2009, 103(1):17-29.

[16] Soheili M, Geological map of Anar, 1:250 000 map, Geological Survey of Iran publication, Tehran, 1981.

[17] Dimitrijevic MD, Geology of the Kerman region. Geological Survey of Iran publication, Tehran. Report, 1973, 52.

[18] Vapnik V, Statistical Learning Theory. New York: Wiley, 1998.

[19] Melgani F, Bruzzone L, Classification of Hyperspectral Remote Sensing Images with Support Vector Machines. IEEE Transaction on Geoscience and Remote Sensing, 2004, 42(8):1778-1790.

[20] Bebis G, Gyaourova A, Singh S, Pavlidis I, Face recognition by fusing thermal infrared and visible imagery. Image and Vision Computing, 2006, 24:727-742.

[21] Ross A, Jain A, Information fusion in biometrics. Pattern Recognition Letter, Elsevier, 2003, 2115-2125.

[22] Fujisada H, Design and performance of ASTER instrument. In: Proceedings of SPIE. The International Society for Optical Engineering, 1995, 2583,16–25.

[23] Yamaguchi Y, Kahle AB, Tsu H, Kawakami T, Pniel M, Overview of Advanced Spaceborne Thermal Emission and Reflection Radiometer (ASTER). IEEE Transactions on Geosciences and Remote Sensing, 1998, 36:1026–1071.

[24] Abrams M, ASTER user handbook. Jet Propulsion Lab, 2002.

[25] Mojedifar S, Ranjbar H, Nezamabadi-pour H, Adaptive Neuro-Fuzzy Inference System application for hydrothermal alteration mapping using ASTER data, Journal of Mining & Environment, 2013, 4(2):83-96.